Solid State Phenomena
ISSN: 1662-9779, Vol. 388, pp 29-37
doi:10.4028/p-x19oZa

Submitted: 2025-12-19
Revised: 2026-02-13
Accepted: 2026-02-20
Online: 2026-04-15

In Situ EBSD Characterisation of Anisotropic Creep Behaviour in a Thick AA2139 Part during in-Forming Artificial Ageing

Gautier Calixte[1,2,a*], Dubos Pierre-Antoine[1,b], Gloaguen David[1,c], Girault Baptiste[1,d] and Rollin Maxime[2,e]

[1]Nantes Université, École Centrale Nantes, CNRS, GeM, UMR 6183, F-44600 Saint-Nazaire, France

[2]Airbus Atlantic, 13 Bd des Apprentis, 44600 Saint-Nazaire, France

[a*]calixte.gautier@univ-nantes.fr, [b]pierre-antoine.dubos@univ-nantes.fr, [c]david.gloaguen@univ-nantes.fr, [d]baptiste.girault@univ-nantes.fr, [e]maxime.m.rollin@airbus.com

Keywords: *in situ* tests, creep-ageing, anisotropy, EBSD, grain misorientations, aluminium alloy.

Abstract. The present study aims to investigate the anisotropic creep behaviour of aluminium alloy 2139 during artificial ageing, through *in situ* thermomechanical loadings under Electron Backscattered Diffraction (EBSD). EBSD analysis enabled the characterisation of microstructural parameters and the identification of grain misorientations which were further correlated with macroscopic creep strain. *In situ* analyses were conducted within a Scanning Electron Microscope (SEM) using a micro-tensile stage that allows simultaneous heating and mechanical loading. Creep tests were performed at 160°C under 50, 100 and 150 MPa along three different orientations in order to investigate the creep behaviour of the alloy. Kernel Average Misorientation (KAM) maps showed a progressive increase of the average KAM values for the different loading conditions, reaching a saturation value after 10 hours. *Ex situ* tensile tests were conducted on creep-aged specimens using Digital Image Correlation (DIC). The main mechanical property evolutions (averaged across all orientations) are a 45 % increase in yield stress, a 10 % increase in ultimate tensile stress and a reduction in ductility, characterised by a notable decrease in elongation. Further works will focus on the result repeatability, as well as on the influence of prior deformation on the creep strain.

Introduction

The age-hardenable aluminium alloy 2139 (AA2139) has been primarily developed for the use in aerospace industry as a high strength and damage tolerant alloy. Current research focusses on improving the aerodynamic and reducing weight of next-generation aircraft by developing complex parts, formed from large and thick raw plates. The forming used in cockpit manufacturing consists of a quasi-static deformation process (press forming) and dynamic process (hydroforming), followed by artificial ageing to strengthen the alloy and reduce residual stresses [1]. The implementation of constitutive equations in a Finite Element Method (FEM) software will enable the optimization of these forming processes, by predicting the final stress state and the springback occurring during machining. During artificial ageing at elevated temperature, the creep phenomenon induces a stress relaxation. Simultaneously, the internal stress state influences the precipitation kinetics, leading to an increase in yield strength and a reduction in creep rate through the hindering of dislocation motion [2]. The present study focuses on the artificial ageing heat treatment. The formed part with a complex internal stress state is heated and held at under-ageing temperature. Experimental creep tests are performed on undeformed micro-samples, to ensure a good control of the stress level and the deformation history in the sample. The objective of this work is to characterise the anisotropic creep-ageing behaviour of thick AA2139 plates in order to understand its relationship with the microstructural evolution occurring during the heat treatment. Although anisotropic creep behaviour and hardening have been studied for various 2xxx series alloys [3], to the best of our knowledge, no study has yet focused on the anisotropic creep behaviour of AA2139, particularly using *in situ* analyses.

Material and Methods

Ex situ calibration of the creep strain

Micro-tensile samples of AA2139 (chemical composition Al-4.86Cu-0.4Mg-0.35Ag-0.29Mn-0.06Si-0.07Fe (wt. %) [4]) in T3 temper were extracted along 0°, 45° and 90° to the Rolling Direction (RD) close to the surface of a 120 mm thick aluminium plate to assess material anisotropy and microstructural features. Macroscopic creep strain at 160°C was first quantified under 0, 100 and 150 MPa using a NewTec MT1000 tensile device with Digital Image Correlation (DIC) under secondary vacuum conditions (Fig. 1). Those experiments were performed to correlate the jaws displacement controlled by the micro-tensile stage with the local strain at gauge section location measured by DIC. The specimen surfaces were covered with a heat resistant white paint with black speckles. Sample heating was provided by two furnaces located under the grip sections of the specimen (Fig. 1(a)). Heating rate was set to 1°C/s. Temperature variations were monitored using a type-K thermocouple and controlled within ± 2.5°C range in the gauge section. Once the target temperature of 160°C was reached, samples were loaded to the initial stress (50, 100 or 150 MPa). Sample alignment with the tensile axis was ensured by glass-ceramic (Macor) hot pins located at the sample shoulders as detailed in (Fig. 1(a)) [1]. Images were acquired at 1-second intervals with a spatial resolution of 3.6 µm/pixel and a field of view of 14.4 × 10.8 mm^2. The DIC processing was achieved using UFreckles software [5] with a Non-Uniform Rational Basis Spline (NURBS) based model and a subset size of 30 pixels. Creep curves were then fitted using a polynomial function in order to reduce the experimental noise.

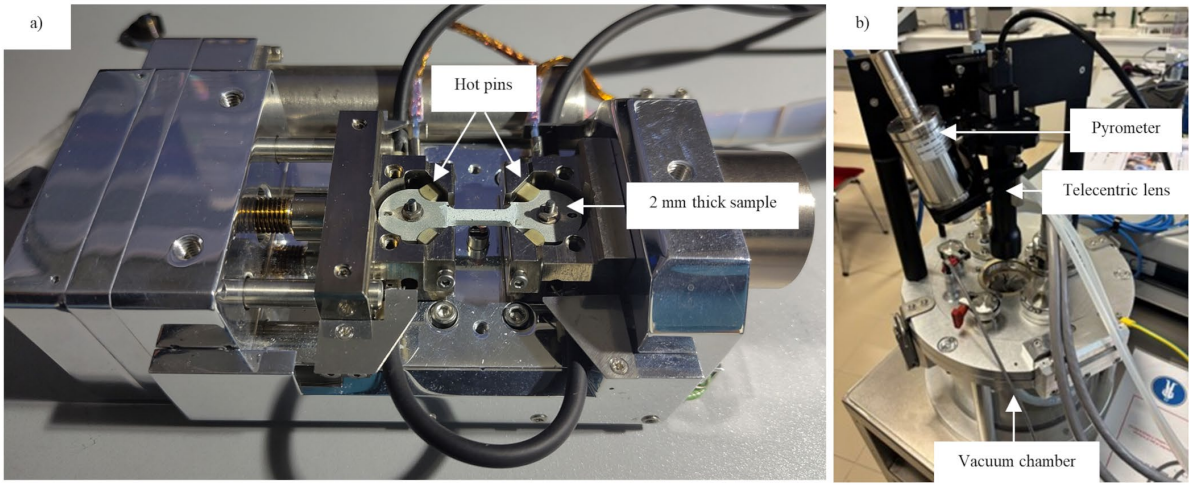

Fig. 1. a) Sample clamping in the tensile stage and b) DIC setup mounted on the vacuum chamber.

In situ creep tests under EBSD

To enable Electron Backscatter Diffraction (EBSD) measurements during *in situ* tests, the upper surface of tensile specimens were ground and polished with a combined Struers LaboPol-30 and LaboForce-100 devices. Successive pre-polishing steps with abrasive diamond (9 µm and 6 µm) ended up by a polishing step using colloidal silica (0.03 µm particle size). Qualitative control of the surface was performed under optical microscope after each step to ensure the complete removal of scratches from the previous steps.

The prepared specimens were subsequently mounted on a MT1000 tensile tester, tilted at 70° inside the chamber of an Ultra High Resolution Tescan Clara Scanning Electron Microscope (SEM) for EBSD measurements with an EDAX Velocity camera (Fig. 2). Creep tests were performed at various loading stresses: 50, 100 and 150 MPa. EBSD acquisitions were automated at 1-hour intervals. Crystal lattice orientations were determined using triplets of Kikuchi bands. If more than one solution is found for a given triplet, a voting scheme is applied to rank the corresponding orientations. The Confidence Index (CI) is then defined by $CI = (V_I - V_{II})/V_{ideal}$, where V_I is the number of votes for the first solution, V_{II} is the number of votes for the second most likely solution and V_{ideal} is the total number of Kikuchi band triplets available [6]. The moderate acquisition rate (1700 diffraction

patterns per second) of the EBSD patterns during mapping resulted in an average CI set between 0.26 and 0.44 with an overall acquisition time of 10 minutes per map. EBSD maps were acquired with a field of view of 1.00 × 0.78 mm^2 and a step size of 1 µm using an electric voltage of 15 keV and a probe current of 40 nA. The space requirement of the tensile stage imposed a working distance of 18 mm. Automation of *in situ* testing included systematic adjustment of the focus, contrast and brightness over a reduced field of view (200 µm) prior to SEM image acquisition for area correlation.

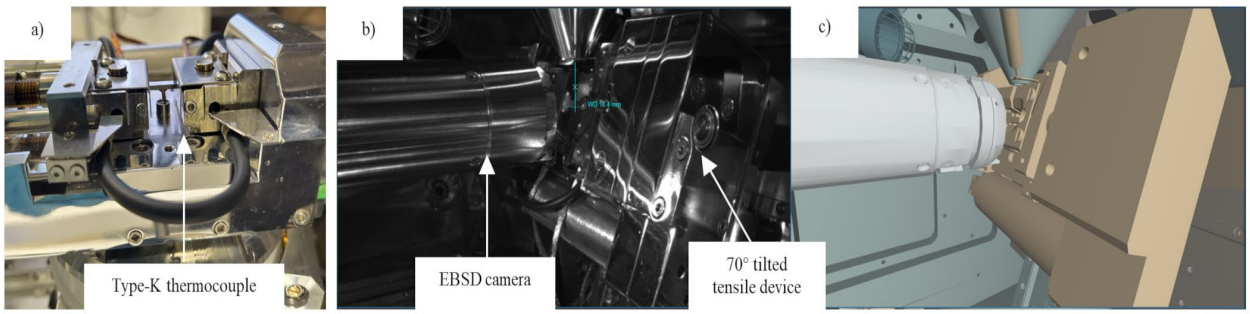

Fig. 2. a) Sample mounting and b) installation of the MT1000 tensile stage tilted at 70° inside the SEM with c) the simulation model developed to avoid collision in the SEM chamber.

Post-processing of the EBSD maps was performed in batches using OIM Analysis V9.1 software. The workflow consisted of reindexation (spherical reindexing and Neighbour Pattern Averaging Reindexing, NPAR) and a two-step cleaning process (grain dilation and CI Standardization). These numerical treatments significantly improved the overall CI values. Fig. 3 shows the Inverse Pole Figures (IPF) of the sample heated to 160°C and subjected to an initial applied stress of 100 MPa along RD. The fraction of points with CI>0.1 increased from 0.493 using the standard Hough indexing to 0.999 after reindexing and cleaning. Similarly, the average CI increased from 0.23 to 0.49.

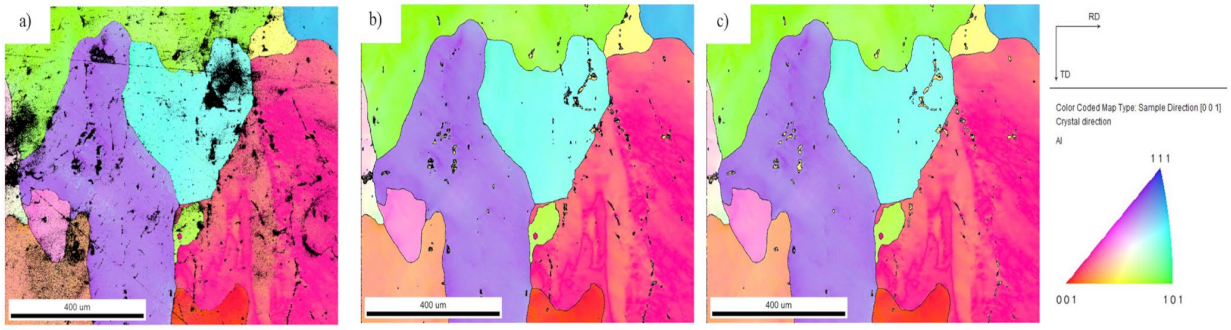

Fig. 3. Inverse Pole Figure maps of AA2139 at 160°C under 100 MPa along RD: a) classical Hough indexing b) spherical reindexing and NPAR and c) spherical reindexing, NPAR and clean-up. RD: Rolling Direction, TD: Transverse Direction.

Tensile tests

To investigate the effect of ageing on the mechanical properties of the alloy and to assess the potential anisotropy, *ex situ* tensile tests combined with DIC have been performed along 0°, 45° and 90° relative to RD, after creep-ageing at 160°C under various applied stresses of 50, 100 and 150 MPa.

Experimental Results

Ex situ creep tests with DIC

Ex situ creep tests were systematically performed prior to *in situ* tests in order to assess creep behaviour under various orientations and loading states, and also to calibrate the strain measured by DIC. An example of the DIC data fitted by a polynomial function is presented in Fig. 4 for the creep curve under 100 MPa applied stress at 45° to RD.

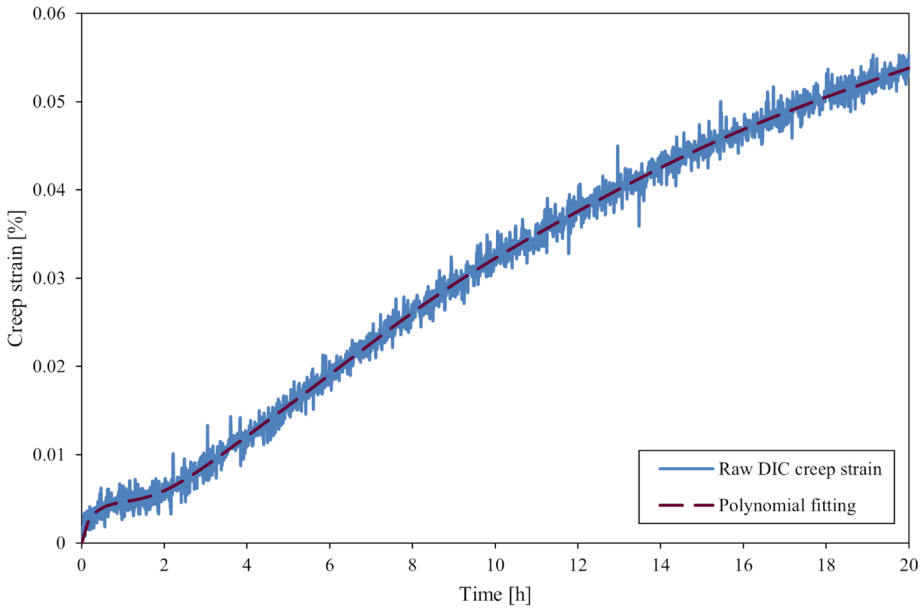

Fig. 4. Polynomial fitting of the DIC calculated creep strain under 100 MPa at 45° to RD.

The complete set of fitted creep curves is presented in Fig. 5. At low stress level (50 and 100 MPa), the RD-oriented samples display higher creep strains than samples along the Transverse Direction (TD). In contrast, this creep strain ranking is no longer valid for a larger stress level (150 MPa), where the sample oriented at 45° to RD exceeds the creep strain of the two other orientations.

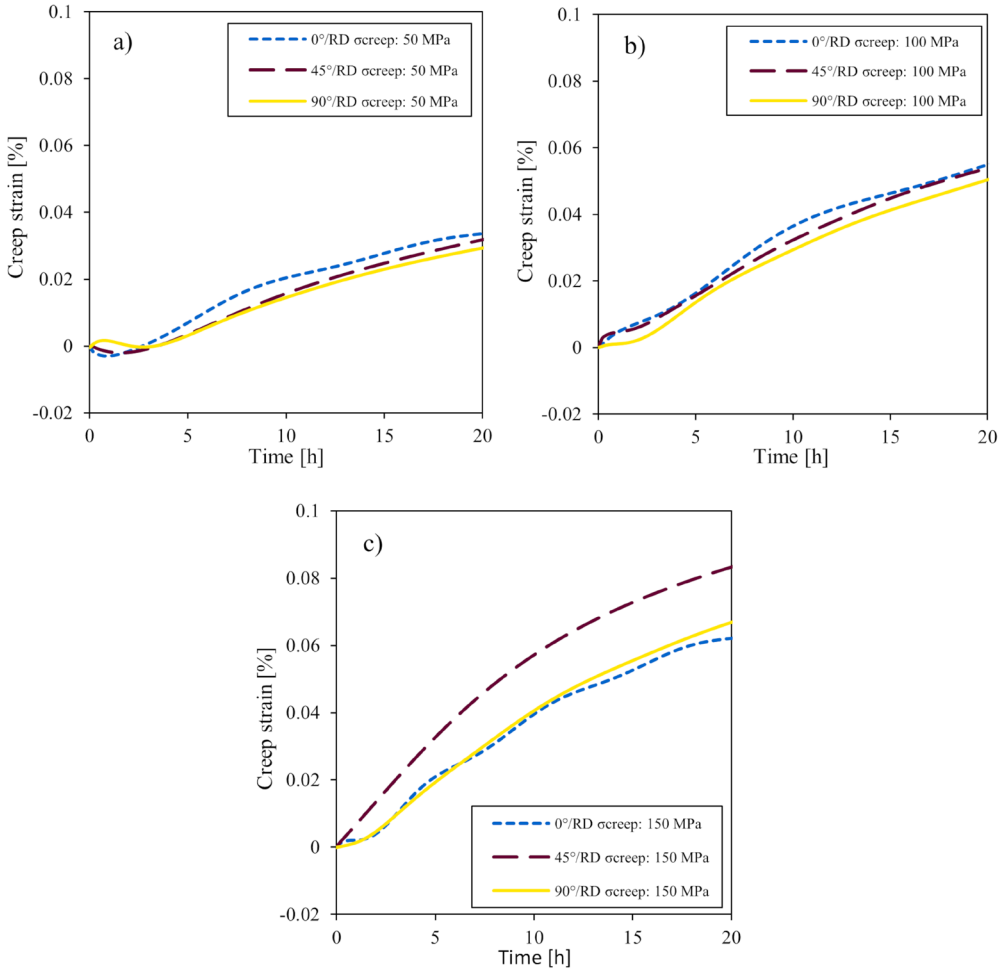

Fig. 5. Creep curves along 0°, 45° and 90° to RD under a) 50 MPa, b) 100 MPa and c) 150 MPa.

In situ creep tests under EBSD

The misorientation analysis was complicated by the large grain size (≈200 µm) of the AA2139 samples. A compromise has thus been made between a large field of view—allowing the analysis over a larger number of grains but inducing long acquisition time—and a reduced 1.00 × 0.78 mm^2 field of view enabling an acquisition time of 10 minutes per EBSD map. This smaller field of view limits the risk of dynamic microstructural changes between the start and the end of the map. A step size of 1 µm was chosen in order to accurately capture the misorientation at the grain boundaries. Fig. 6 shows the evolution of Kernel Average Misorientation (KAM) during the creep tests under 50, 100 and 150 MPa along RD. The measured misorientation is directly related to the presence of dislocations and precipitate formation. From onset of creep-ageing, misorientations are heterogeneously distributed across the maps. The heterogeneity increases as the creep progresses suggesting that some grain orientations would be more likely to promote precipitate formation.

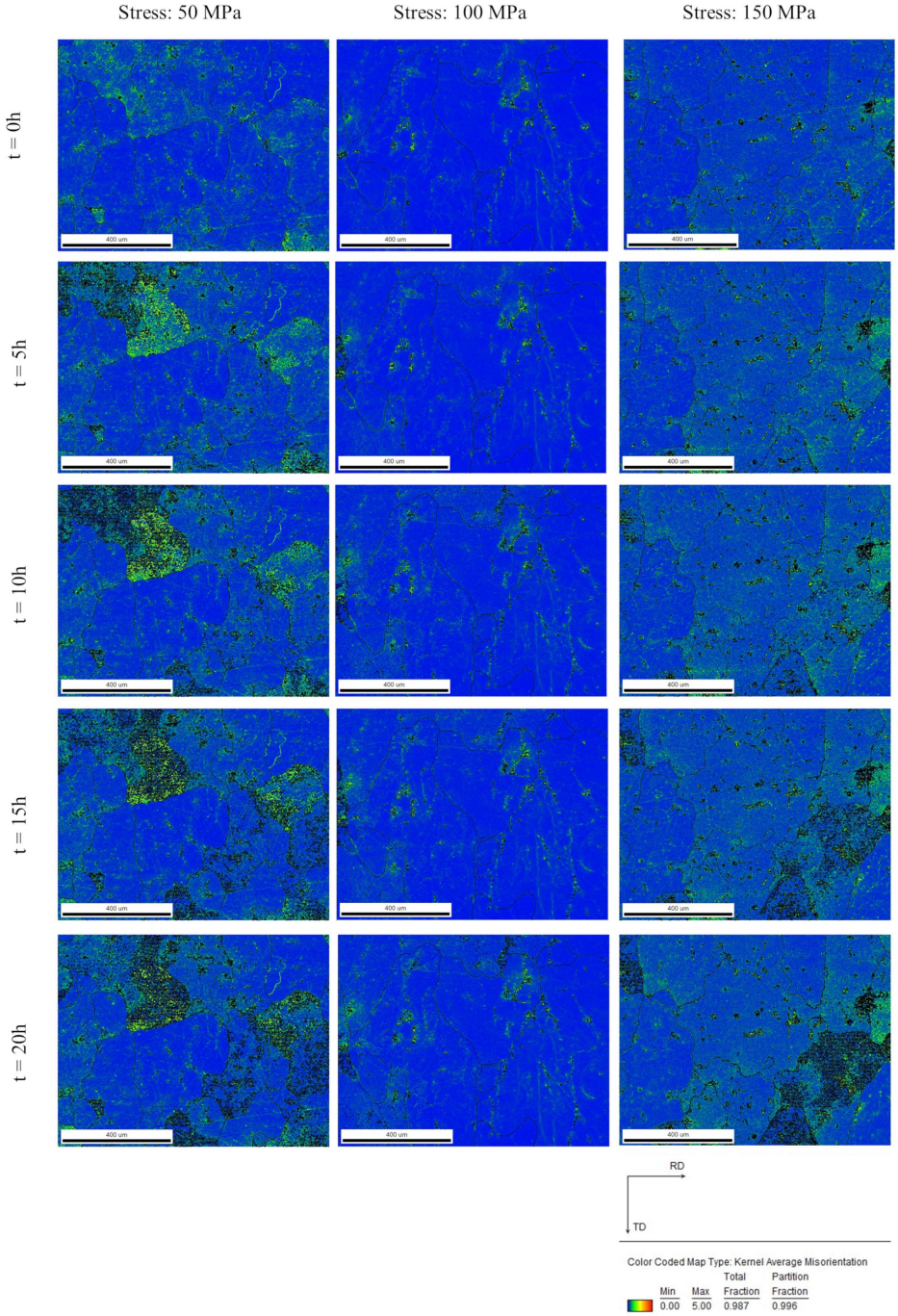

Fig. 6. KAM maps during creep ageing under 50, 100 and 150 MPa along RD at different creep times. Points with CI<0.1 are shown in black.

To quantify the misorientation evolutions during ageing, the average KAM value was calculated for each EBSD map. These values were normalized by the maximum value of each creep test. Their evolutions are presented in Fig. 7. Saturation is reached after 10 hours regardless of the applied stress. The symbols represent the experimental data points contained in the KAM maps. The lines correspond to the modelled evolution of the average KAM values. Most of the misorientations develop during the first 5 hours, which is consistent with the formation kinetics of Ω and θ' precipitates reported in the literature [4, 7-8]. As precipitates nucleate and grow, they effectively block dislocations. The observed saturation suggests a dynamic equilibrium in which dislocation nucleation is balanced by recovery mechanisms activated at the creep temperature.

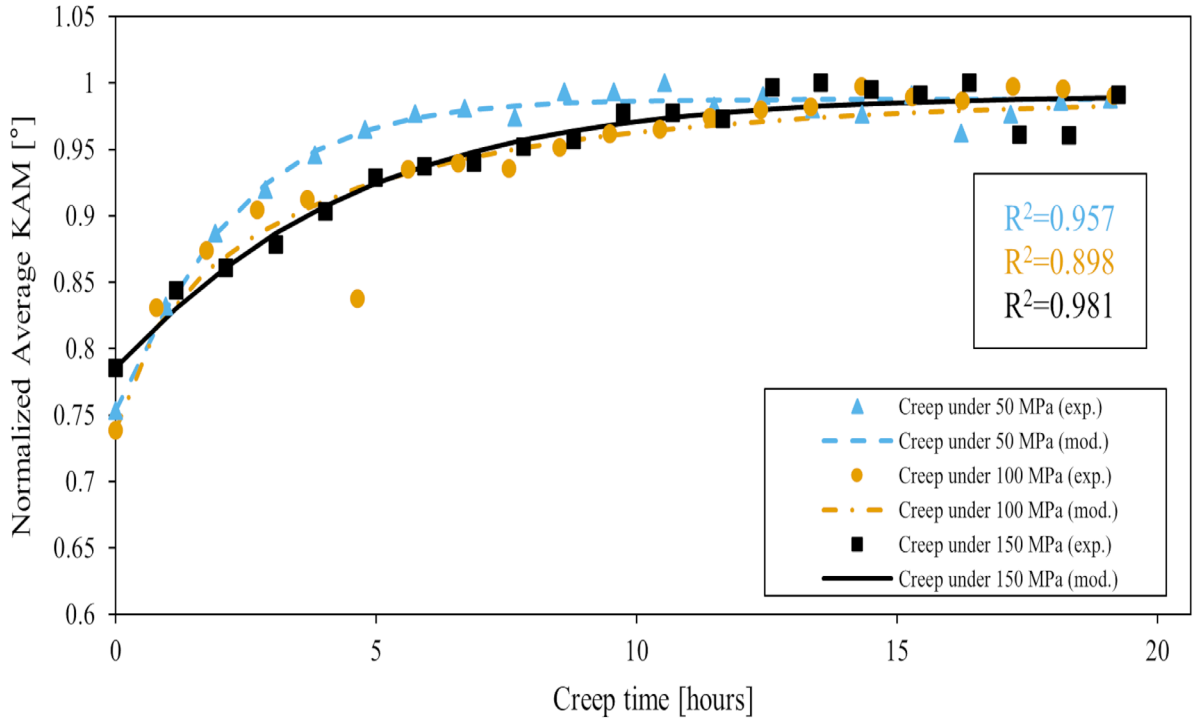

Fig. 7. Evolution of the averaged KAM values during creep tests under 50, 100 and 150 MPa along RD.

Fig. 6 and Fig. 7 shows an earlier rise in the average misorientation during creep under low stress (50 MPa) compared with higher stresses. Although the creep strain rate is generally expected to increase with applied stress [3], the precipitation of strengthening phase has been found to be delayed when Al-Cu-Mg-Ag samples were aged under external stress with the promotion of θ' precipitates at the expense of Ω [9]. This stress-dependent precipitation behaviour may contribute to the observed differences in KAM evolution.

Tensile tests post creep ageing

Ex situ tensile tests were conducted along 0°, 45° and 90° to RD after creep-ageing. DIC was performed and processed with the UFreckles software to evaluate the macroscopic strain and the evolution of mechanical properties through virtual longitudinal and transversal extensometers. Fig. 8 shows tensile curves in the T3 state and after creep-ageing along RD. The main effect of the creep ageing is a significant Yield Stress (YS) increase and a moderate Ultimate Tensile Stress (UTS) enhancement (Fig. 9(a)). The gap reduction between YS and UTS indicates a loss of work-hardening capability leading to an earlier and more sudden necking. UTS rise is more pronounced for samples subjected to creep under higher applied stresses.

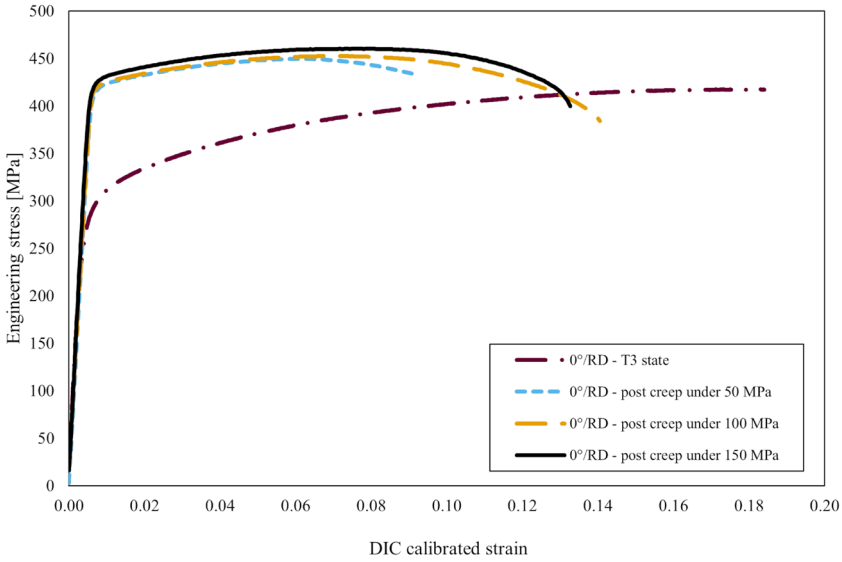

Fig. 8. Tensile test along RD after creep ageing under 50, 100 and 150 MPa.

Precipitate formation is promoted by dislocation density, particularly semi-coherent θ' precipitates [9-11]. Fig. 9 summarizes the results tensile tests on creep-aged samples. For each applied stress level, data were averaged over the three orientations according to Eq. 1 where X is the considered quantity:

$$X_{100\ \mathrm{MPa}} = \left(X_{100\ \mathrm{MPa}_{/\mathrm{RD}}} + 2X_{100\ \mathrm{MPa}_{/45°}} + X_{100\ \mathrm{MPa}_{/\mathrm{TD}}}\right)/4\ . \quad (1)$$

Fig. 9(c) highlights the evolution of plastic anisotropy after creep-ageing. While the T3 state exhibits an averaged r-value (Lankford coefficient) of 0.76, creep-ageing at 160°C results in a slight shift towards isotropy (r=1). The reduction in ductility, highlighted by the elongation drop after creep-ageing in Fig. 9(d) reflects the ability of precipitates to hinder dislocation motion.

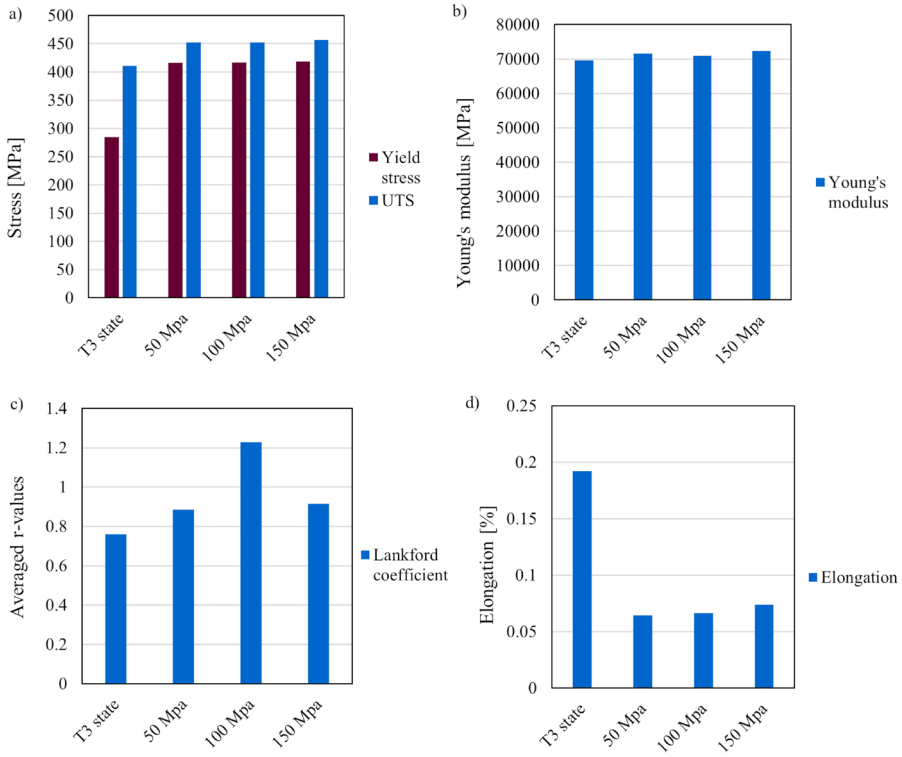

Fig. 9. Tensile tests summary averaged along the three directions a) Yield stress and Ultimate Tensile Stress, b) Young's modulus, c) Lankford coefficient and d) elongation.

Summary

Ex and *in situ* creep tests within the SEM were performed on AA2139 at 160°C under various loadings conditions to investigate the creep behaviour of the alloy and the related microstructural evolutions. The main findings can be summarized as follows:

- Creep strains measured by DIC exhibit a moderate anisotropy at 160°C. The initial stress increase resulted in a higher creep strain, regardless of the orientation.
- *In situ* tests under EBSD enabled the quantification of the average KAM in a 1.00×0.78 mm^2 field of view. The normalized average KAM value reached a saturation value after 10 hours.
- *Ex situ* tests on creep-aged samples highlighted the impact of creep-ageing on the mechanical properties. All the three tested orientations exhibited an average increase of 45 % of the initial yield stress and an average increase of 10 % of the ultimate tensile stress.
- The creep-ageing promotes precipitate formation. These precipitates hinder dislocation motion and reduce the ductility. The elongation after creep-ageing showed a dispersion over the tensile tests, but all samples exhibited reductions of 20-60 % as compared to T3 samples.

The study focused on microstructure evolution during *in situ* creep tests under EBSD. While the results reveal clear trends in anisotropic creep behaviour and precipitation-related misorientation development, the limited number of tests per configuration remains a constraint, particularly regarding the variability observed between orientations. In the next phase of this work, a larger test campaign will be conducted to characterize the creep behaviour of the alloy taking into account the impact of repeatability. Future works will focus on the transformation strain measurement (creep test performed under zero stress) and the investigation of the impact of prior static and dynamic deformation on the creep behaviour. These complementary studies will contribute to the development of physically based constitutive equations for accurate creep-ageing modelling.

Declaration of Competing Interest

The authors declare that they have no known competing financial interests or personal relationship that could have appeared to influence the work reported in this paper.

Acknowledgement

The authors gratefully acknowledge Airbus Atlantic and the ANRT (French National Association for Research and Technology) for funding C. Gautier's PhD thesis.

References

[1] A.D. Smith, D. Lunt, M. Taylor, A. Davis, R. Thomas, F. Martinez, A. Candeias, A. Gholinia, M. Preuss, J.M. Donoghue, A new approach to SEM in-situ thermomechanical experiments through automation, Ultramicroscopy. 280 (2026).

[2] K. C. Ho, J. Lin and T. A. Dean, Constitutive modelling of primary creep for age forming an aluminium alloy, J. Mater. Process. Technol. 153-154 (2004) 122-127.

[3] X. Wang, Z. Shi, J. Lin, A generalised framework for modelling anisotropic creep-ageing deformation and strength evolution of 2xxx aluminium alloys, Int. J. Plast. 182 (2024).

[4] D. Bakavos, P.B. Prangnell, B. Bes, F. Eberl, The effect of silver on microstructural evolution in two 2xxx series Al-alloys with a high Cu:Mg ratio during ageing to a T8 temper, Mater. Sci. Eng. A. 491 (2008) 214-223.

[5] J. Rethore (2018). UFreckles (v.2.0). Zenodo. https://doi.org/10.5281/zenodo.1433776.

[6] D. P. Field, Recent advances in the application or orientation imaging, Ultramicroscopy. 67 (1997) 1-9.

[7] H. So, S.J. Won, J. Park, S.J. Oh, L. Kang, K.H. Kim, Mechanical properties and microstructural evolution in Al-Cu-Mg-Ag alloy with a $Cu_xMg_{x/10}$ content, Mater. Sci. Eng. A. 824 (2021).

[8] J. Fan, B. Yang, Y. Wang, M. Gao, R. Guan, Enhancing the tensile strength and heat resistance induced by high-density Ω phases in an Al-Cu-Mg-Ag alloy, JMR&T. 18 (2022) 3347-3357.

[9] X.Y. Liu, Q.L. Pan, X.L. Zhang, S.X. Liang, L.Y. Zheng, F. Gao, H.L. Xie, Effect of stress-ageing on the microstructure and properties of an aging forming Al-Cu-Mg-Ag alloy, Mater. Des. 58 (2014) 247-251.

[10] Y. Xu, L. Zhan, W. Li, Effect of pre-strain on creep ageing behavior of 2524 aluminum alloy, J. Alloys Compd. 619 (2017) 564-571.

[11] Y. Yang, L. Zhan, R. Shen, X. Yin, X. Li, W. Li, M. Huang, D. He, Effect of pre-deformation on creep age forming of 2219 aluminum alloy: Experimental and constitutive modelling, Mater. Sci. Eng. A. 683 (2017) 227-235.

[12] S. Cui, C. Zhang, M. Liu, L. Chen, G. Zhao, Precipitation behavior of an Al-Cu-Li-X alloy and competing relationship among precipitates at different ageing temperatures, Mater. Sci. Eng. A. 814 (2021).